Research Article

Chunwei Zhang*, Qiao Jin, Yansheng Song, Jingli Wang, Li Sun*, Haicheng Liu, Limin Dun, He Tai, Xiaodong Yuan, Hongmei Xiao, Limeng Zhu, and Songlin Guo

Vibration analysis of a sandwich cylindrical shell in hygrothermal environment

https://doi.org/10.1515/ntrev-2021-0026
received March 28, 2021; accepted April 22, 2021

Abstract: The sandwich structures are three- or multi-layered structures such that their mechanical properties are better than each single layer. In the current research, a three-layered cylindrical shell including a functionally graded porous core and two reinforced nanocomposite face sheets resting on the Pasternak foundation is used as model to provide a comprehensive understanding of vibrational behavior of such structures. The core is made of limestone, while the epoxy is utilized as the top and bottom layers' matrix phase and also it is reinforced by the graphene nanoplatelets (GNPs). The pattern of the GNPs dispersion and the pores distribution play a crucial role at the continuous change of the layers' properties. The sinusoidal shear deformation shells theory and the Hamilton's principle are employed to derive the equations of motion for the mentioned cylindrical sandwich shell. Ultimately, the impacts of the model's geometry, foundation moduli, mode number, and deviatory radius on the vibrational behavior are investigated and discussed. It is revealed that the natural frequency and rotation angle of the sandwich shell are directly related. Moreover, mid-radius to thickness ratio enhancement results in the natural frequency reduction. The results of this study can be helpful for the future investigations in such a broad context. Furthermore, for the pipe factories current study can be effective at their designing procedure.

Keywords: vibration, sandwich cylindrical shell, porous materials, graphene nanoplatelets, hygrothermal environment, sinusoidal shear deformation

1 Introduction

Structural analyses attracted higher levels of scholars' attention nowadays. Among them, sandwich structures are well-known due to their high level of functionality. These structures are broadly implemented in ships, aerospace vehicles, and cargo containers. The porous type of sandwich structures meets extensive applications due to their lower weight to stiffness ratio. For instance, in the aircraft industries, aircraft with higher speed and stiffness and lower weight is accessible by the means of sandwich panels [1–4]. Depending on their application, sandwich structures may include three or more layers. Catania *et al.* [5] studied the mechanical damping behavior of multilayer components due to their wide range of applications. In their work, the results are validated by an experimental test. Beside this, plasma techniques are used by Rongong *et al.* [6] to generate constrained layer damping coatings on the metallic substrates. Also, in another work, Yu *et al.* [7] discussed the damping efficiency of the coating system based on the Reuss model and Hashin–shtrickman equation. In their work, the theoretical results showed that for a coating system, there is an optimum thickness of the coating layer that causes the coating structure obtain the best balance between the strength and the damping capacity. In two different works, Amir and his coresearchers [8,9] presented their findings of vibrational behavior of three-layered circular and annular plates, in which a rheological fluid core was put between two magnetostrictive face sheets. More recent sandwich structures exploit a core that is constituted of porous material to gain a lighter structure.

* **Corresponding author: Chunwei Zhang,** School of Civil Engineering, Structural Vibration Control Group, Qingdao University of Technology, Qingdao, China, e-mail: zhangchunwei@qut.edu.cn
* **Corresponding author: Li Sun,** School of Civil Engineering, Shenyang Jianzhu University, Shenyang, China, e-mail: sunli@sjzu.edu.cn
Qiao Jin, Yansheng Song, Jingli Wang, Haicheng Liu: School of Civil Engineering, Shenyang Jianzhu University, Shenyang, China
Limin Dun, He Tai: Shenyang Geotechnical Investigation & Surveying Research Institute Co., Ltd, Shenyang, China
Xiaodong Yuan: CSCEC Capital Holding, China State Construction Engineering Group Co., Ltd, Beijing, China
Hongmei Xiao, Limeng Zhu, Songlin Guo: School of Civil Engineering, Structural Vibration Control Group, Qingdao University of Technology, Qingdao, China

Furthermore, functionally graded materials (FGMs) are a new branch of elaborated engineering composite materials [10,11] that attracted the scientists' attention. The layers constituted from FGMs are fully metallic at the bottom surface and fully ceramic at the top surface or *vice versa*. FGMs are first introduced by Koizumi [12]. Liu *et al.* [13] broadened our knowledge about FGMs by working on the wave propagation using a numerical technique. In another work, Han *et al.* [14] numerically studied FGMs' transient wave propagation using another method. In 2002, Najafizadeh and Eslami [15] examined buckling the behavior of a circular FGM plate under radial loading. Arshid and Khorshidvand [16] examined the vibrational behavior of a saturated porous FG circular plate patched to piezoelectric face sheets using a differential quadrature method (DQM). One of the first works on the sandwich cylindrical shells dates back to 1995, in which Huang and Dasgupta [17] investigated the composite cylindrical shells to explain their free vibration behavior. After that, laminated cylindrical shells have been considered as a model to investigate static bending behavior under various boundary conditions using the differential cubature method [18]. In more recent years, the bending behavior of cylindrical sandwich panels has been evaluated by Pydah and Batra [19], who succeed to present an analytical solution for the mentioned bending behavior. In 2019, Sun *et al.* [20] experimentally investigated the different dynamic responses of the sandwich panels. They aimed to present a thorough guideline for the fabrication of sandwich panels with a higher ratio of blast protection capacity to weight. Electromechanical systems are exposed to different electrical and mechanical loadings and require a comprehensive study due to their important parameters. By the growth of the application of sandwich plates, more accurate plate theories are needed to obtain responses with higher accuracy. In the past decades, the FG plates and shells have been often analyzed using the first order shear deformation theory (FSDT) or higher order theories [21–24]. As an example, Trabelsi *et al.* [25] used modified FSDT to examine the thermal buckling of the FG plates and cylindrical shells. Based on the nonlocal elasticity theory, Ke *et al.* [26] took a nano piezoelectric cylindrical shell into consideration and investigated its vibrational behavior. They employed Love's theory which is usually used for thin shells and also used DQM for solving the obtained differential equations. In a similar study, Razavi *et al.* [27] conducted a research on electromechanical vibrational response of nano cylinders. They derived the governing equations with the aid of the energy method and Hamilton's principle and captured the size effect *via* the couple stress theory. As another instance, Khoa *et al.* [28] employed a cylindrical panel model which was reinforced by single-walled carbon nanotubes (SWCNTs) to study the vibrations of the functionally graded carbon nanotube-reinforced composite (FG-CNTRC) cylindrical shells. For integrity, they applied the thermal environment on the entire structures and used higher-order shear deformation theory (HSDT). Nanoparticles and especially CNTs and graphene nanoplatelets (GNPs) specifications are discussed in numerous researches, recently [29–33]. Single-layered graphene sheets' mechanical behavior and especially their buckling response, regarding the scale-effect, is considered by Fattahi *et al.* [34,35]. They attained the governing equations based on classical theory, FSDT, and HSDT. As another attempt, forced and free vibrational behaviors of a viscoelastic core equipped with GNPs-reinforced face sheets are examined by Mohseni and Shakouri [36]. They assumed face sheets are FG due to different types of GNPs distributions. A developed HSDT was applied to provide an analytical solution for the buckling capacity of sandwich plates containing cores with and without the GNPs reinforcement phase [37]. Moreover, free vibration and buckling analysis of cylindrical shells and sandwich plates is addressed by Kumar and Srinivasa [38]. After that, Ibrahim *et al.* [39] used FSDT to analyze the mechanical responses of FGM panels. Furthermore, Mehar and Panda [40] employed the finite element method to evaluate the temperature dependency of vibrational behavior of sandwich curved panel reinforced by functionally graded carbon nanotubes (FG-CNTs). In their paper, HSDT is used to derive displacement field equations. More recently, Karimiasl *et al.* [41] applied HSDT to assess doubly curved flexible core integrated with piezoelectric layers as a model to address the nonlinear vibration analysis. They concluded that an increment in the shaped memory alloys (SMA) volume fraction declined the frequency. Furthermore, the elasto-dynamic behavior of cylindrical tubes is evaluated by Ramezani and Mirzaei [42]. They assumed their model under moving pressures and different boundary conditions. In 2014, a new quasi-3D hyperbolic shear deformation theory for vibrational responses is proposed by Hebali *et al.* [43] to get more accurate results. This theory accounts for the stretching and shear deformation effects and eliminates their dependency on shear correction factor. Mirjavadi *et al.* [44] carried out a study on forced vibration of annular sector plates which are composed of the nanocomposite. They employed More–Tanaka approach to determine the material properties. In another study [45], they provided similar research, but for conical shells, and investigated the effect of

different parameters on the results. Three types of porosity distributions are considered by Safaei [46] to analyze a multilayered sandwich plate whose core is made from porous materials. He used finite element method to obtain the results. Next, Sahmani *et al.* [47] provided a closed-form solution for examining vibrational response of small-scaled beams that are made from GNPs-reinforced composites. They derived the motion equations *via* HSDT to take the shear deformations into account. Moreover, they conducted another study [48] to consider the effect of size on the post-buckling behavior of plates that were reinforced by GNPs. Different types of GNPs dispersion patterns are considered by them. Most recently, Arshid and Amir [49] provided an investigation on the thermal buckling of porous-reinforced nanocomposite structures and concluded that adding GNPs to the structure may increase or decrease the critical buckling temperature, depending on their dispersion patterns. Beside this, Fan *et al.* [50] used modified couple stress theory (MCST) and examined the nonlinear oscillations of porous FG plates in nanoscale. They used NURBS-based isogeometric approach to gain the results. Wang *et al.* [51] performed nonlinear vibration analysis of porous shells that were reinforced with GNPs. They employed an improved Donnell nonlinear shell theory to formulate their model. A general approach is provided for the free vibration analysis of rotating functionally graded carbon nanotube-reinforced composite (FG-CNTRC) cylindrical shells with arbitrary boundary conditions by Qin *et al.* [52] based on FSDT. Also, a comparison study is presented by Qin *et al.* [53] on free vibrations of cylindrical shell with various boundary conditions using numerical methods. Shen *et al.* [54] considered effect of thermal environment on nonlinear vibration of functionally graded graphene nanoplatelets (FG-GNPs)-reinforced laminated cylindrical shells.

In the present paper, a sandwich cylindrical structure including FG porous core integrated by the GNPs-reinforced composites (GNP-RC) layers is considered as model to provide a comprehensive insight on its vibrational behavior. In the previously published papers, the sandwich cylindrical model with such exclusive configuration is not examined, yet. The sandwich structure is rested on the Pasternak foundation and the whole model is placed in a hygrothermal environment. As sinusoidal shear deformation shells theory (SSDST) is more accurate than lower-order theories, it is hired to gain more reliable results. Based on the Hamilton's principle and variational approach, the equations of motion are derived and analytically solved. Finally, the influences of various parameters as porosity coefficient index and their distribution patterns, GNPs volume fraction index, and their dispersion types, geometry, mode number, and the moduli of foundation on the natural frequency of presented sandwich cylindrical shell are evaluated. The results could help in obtaining a deeper understanding of these structures which can be helpful in different industries, such as, automobiles, micro electro mechanical system (MEMS) processes, and aerospace.

2 Mathematical modeling

According to the cross-sectional view in Figure 1, the proposed model is a cylindrical sandwich shell including an FG porous core confined by two GNP-RC face sheets

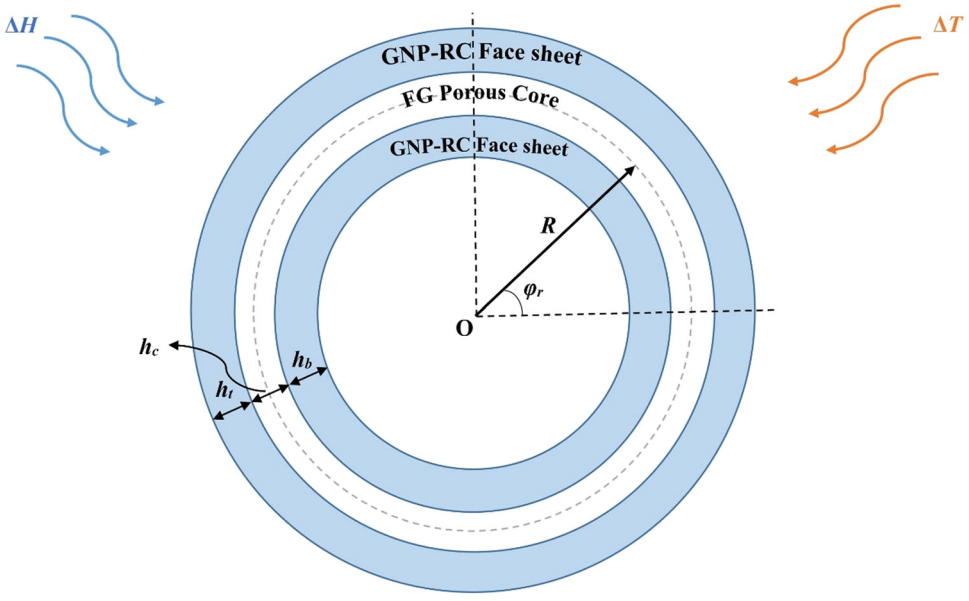

Figure 1: Cross-section view of the sandwich cylindrical shell subjected to hygrothermal loads.

with mid-radius of R, length of L, and rotation angle of φ_r resting on Pasternak elastic foundation. The structure is entirely subjected to hygrothermal loading. Also, h_c, h_t, and h_b denote representatives of the z direction width of the porous core, top, and bottom skins. Moreover, the sum of the height of different parts serves as h representing the total height of the sandwich model. In the intermediate-plane of the shell, the cylindrical coordinate system (x, θ, z) is placed at the corner point in which x, θ, and z are axial, circumferential, and thickness directions of the model, respectively.

Strain components can be obtained by SSDST. Accordingly, the displacements of an arbitrary point either in porous core or in GNPs-RC face sheets can be presented as [55]:

$$\begin{aligned} u(x,\theta,z,t) &= u_0(x,\theta,t) + f(z)\lambda_x(x,\theta,t) \\ &\quad - g(z)\frac{\partial}{\partial x}w_0(x,\theta,t), \\ v(x,\theta,z,t) &= v_0(x,\theta,t) + f(z)\lambda_\theta(x,\theta,t) \\ &\quad - \frac{1}{R}g(z)\frac{\partial}{\partial \theta}w_0(x,\theta,t), \\ w(x,\theta,z,t) &= w_0(x,\theta,t) \end{aligned} \tag{1}$$

where u, v, and w are the movement components in the longitudinal, radial, and thickness direction, respectively. Moreover, u_0, v_0, and w_0 represent the movement components on the intermediate-plane; λ_x and λ_θ denote the rotation about θ and x-axes, respectively. Furthermore, $f(z)$ and $g(z)$ can be determined by SSDST as:

$$f(z) = (h/\pi)\sin(\pi z/h), \quad g(z) = z \tag{2}$$

Based on the Von Karman's assumptions, strain field can be derived as [56,57]:

$$\begin{aligned} \varepsilon_{xx} &= \frac{\partial}{\partial x}u(x,\theta,z,t), \\ \varepsilon_{\theta\theta} &= \frac{1}{R}\left(\frac{\partial}{\partial \theta}v(x,\theta,z,t) + w_0(x,\theta,z,t)\right), \\ \gamma_{x\theta} &= \frac{\partial}{\partial x}v(x,\theta,z,t) + \frac{1}{R}\frac{\partial}{\partial \theta}u(x,\theta,z,t), \\ \gamma_{xz} &= \frac{\partial}{\partial x}w(x,\theta,z,t) + \frac{\partial}{\partial z}u(x,\theta,z,t), \\ \gamma_{\theta z} &= \frac{1}{R}\frac{\partial}{\partial \theta}w(x,\theta,z,t) + \frac{\partial}{\partial z}v(x,\theta,z,t) \end{aligned} \tag{3}$$

By inserting displacement components of equation (1) into equation (3), the strains can be obtained based on the SSDST.

The stresses related to the core and face sheets in the hygrothermal environment can be presented by ref. [58,59]:

$$\begin{Bmatrix} \sigma_{xx} \\ \sigma_{\theta\theta} \\ \sigma_{\theta z} \\ \sigma_{xz} \\ \sigma_{x\theta} \end{Bmatrix} = \begin{bmatrix} C_{11i} & C_{12i} & 0 & 0 & 0 \\ C_{12i} & C_{22i} & 0 & 0 & 0 \\ 0 & 0 & C_{44i} & 0 & 0 \\ 0 & 0 & 0 & C_{55i} & 0 \\ 0 & 0 & 0 & 0 & C_{66i} \end{bmatrix} \times \begin{Bmatrix} \varepsilon_{xx} - \alpha_{11i}\Delta T - \beta_{11i}\Delta H \\ \varepsilon_{\theta\theta} - \alpha_{22i}\Delta T - \beta_{22i}\Delta H \\ \gamma_{\theta z} \\ \gamma_{xz} \\ \gamma_{x\theta} \end{Bmatrix}; \quad i = c, f \tag{4}$$

where C denotes the elastic coefficients and subscript c and f represent the porous core and GNP-RC face sheets, respectively. Moreover, α and β represent the coefficients related to thermal expansion and moisture expansion. ΔT and ΔH are the temperature alternation and moisture changes, one after another. A porous layer, made of Limestone, is used whose elastic coefficients can be written as [43]:

$$\begin{aligned} C_{11c} = C_{22c} &= \frac{E_c(z)}{(1+\nu_c)(1-\nu_c)}, \\ C_{12c} = C_{21c} &= \frac{\nu_c E_c(z)}{(1+\nu_c)(1-\nu_c)}, \\ C_{44c} = C_{55c} = C_{66c} &= \frac{E_c(z)}{2(1+\nu_c)} \end{aligned} \tag{5}$$

where $E_c(z)$ and ν_c indicate Young's elasticity modulus and Poisson's ratio, respectively. The type of core porosity distribution is responsible for elastic coefficients variations.

In fact, the philosophy of pores' presence is to help the weight reduction without having a considerable destructive impact on the mechanical properties of the whole sandwich model. It is revealed that the presence of pores inside the core results in lower magnitude of mechanical properties reduction in comparison with their presence within the face sheets. So, they assumed to exist only within the core layer. For even type of porosity distribution, pores become distributed symmetrically and elasticity modulus, density, and hygrothermal expansion coefficients distributions will be [60]:

$$E_c(z) = E_0[1 - p\ \cos(\pi z/h_c)], \tag{6a}$$

$$\begin{aligned} &\{\rho_c(z),\ \alpha_c(z),\ \beta_c(z)\} \\ &= \{\rho_0,\ \alpha_0,\ \beta_0\}[1 - p_m\ \cos(\pi z/h_c)] \end{aligned} \tag{6b}$$

Where subscript 0 is the sign to address the material properties of the perfect layer. Also, p and p_m are porosity and mass density coefficients which can be defined as [61]:

$$p = 1 - \frac{E_2}{E_1}, \quad p_m = 1 - \frac{\rho_2}{\rho_1} = 1 - \sqrt{1-p} \tag{7}$$

E_1, E_2, and ρ_1, ρ_2 are maximum and minimum magnitudes of Young's modulus and maximum and minimum magnitudes of the density of the porous core, respectively. On the other hand, for uneven porosity distributions, pores distribution is asymmetrical with respect to the intermediate-plane thus [62]:

$$E_c(z) = E_0[1 - p\ \cos(\{(0.5\pi/h_c)(z + 0.5h_c)\})], \tag{8a}$$

$$\{\rho_c(z),\ \alpha_c(z),\ \beta_c(z)\} = \{\rho_0,\ \alpha_0,\ \beta_0\}[1 - p_m\ \cos(\{(0.5\pi/h_c)(z + 0.5h_c)\})] \tag{8b}$$

At the end, for uniformly distributed porosity, elasticity modulus and density are thickness independent as [46]:

$$E_c(z) = E_0[1 - p\zeta], \tag{9a}$$

$$\{\rho_c(z),\ \alpha_c(z),\ \beta_c(z)\} = \{\rho_0,\ \alpha_0,\ \beta_0\}\sqrt{1 - p_m\zeta} \tag{9b}$$

in which:

$$\zeta = [1 - (2\{\sqrt{1-p} - 1\}/\pi + 1)^2]/p \tag{10}$$

To determine the elastic coefficients for the FG-GNP-RC face sheets, the following relations can be represented [63]:

$$\begin{aligned} C_{11f} &= C_{22f} = (1 - \nu_f(z))E_f(z)/[(1 + \nu_f(z))(1 - 2\nu_f(z))], \\ C_{12f} &= C_{21f} = \nu_f(z)E_f(z)/[(1 + \nu_f(z))(1 - 2\nu_f(z))], \\ C_{44f} &= C_{55f} = C_{66f} = E_f(z)/2(1 + \nu_f(z)) \end{aligned} \tag{11}$$

Top and bottom physical properties are also variable through their thicknesses. To determine the effective values of these parameters for different models, Halpin–Tsai and MR micromechanical models are employed. Halpin–Tsai model uses the following relation to predict the effective Young's modulus [64]:

$$E_f(z) = \frac{E_M}{8}\left[3\left(\frac{1 + \zeta_L\eta_L V_{GNP}}{1 - \eta_L V_{GNP}}\right) + 5\left(\frac{1 + \zeta_W\eta_W V_{GNP}}{1 - \eta_W V_{GNP}}\right)\right] \tag{12}$$

in which E_M denotes matrix part Young's modulus; while the volume fraction of GNPs is shown by V_{GNP}. Furthermore, ζ_L, ζ_W, η_L, and η_W state properties of the GNPs, which is related to its geometry, and can be defined as [65]:

$$\begin{aligned} \zeta_L &= 2\left(\frac{l_{GNP}}{t_{GNP}}\right), \quad \eta_W = \left[\left(\frac{E_{GNP}}{E_M}\right) - 1\right]\Big/\left[\left(\frac{E_{GNP}}{E_M}\right) + \zeta_W\right], \\ \zeta_W &= 2\left(\frac{w_{GNP}}{t_{GNP}}\right), \quad \eta_L = \left[\left(\frac{E_{GNP}}{E_M}\right) - 1\right]\Big/\left[\left(\frac{E_{GNP}}{E_M}\right) + \zeta_L\right] \end{aligned} \tag{13}$$

Here, l_{GNP} denotes the GNPs' length, their thickness is shown by t_{GNP}, and their width is represented by w_{GNP}. Moreover, E_{GNP} is Young's modulus of GNPs reinforcements. Noteworthy, the GNPs' volume fraction added to volume fraction of matrix portion should be 1 and that of GNPs can be obtained *via* the following equation [66]:

$$V_{GNP} = \frac{g_{GNP}(z)}{g_{GNP}(z) + (\rho_{GNP}/\rho_M)(1 - g_{GNP}(z))} \tag{14}$$

In the abovementioned relation, ρ is the density. The subscripts GNP and M are related to the GNPs reinforcements and matrix. Also, g_{GNP} refers to the dispersion pattern of the reinforcement phase weight fraction and can be presented as [67]:

Parabolically dispersed GNPs through the matrix:

$$g_{GNP}(z) = \frac{4}{h_f^2}\mu_P W_{GNP} z^2; \tag{15a}$$

Linearly dispersed GNPs through the matrix

$$g_{GNP}(z) = \mu_L W_{GNP}\left(\frac{1}{2} \pm \frac{z}{h_f}\right); \tag{15b}$$

Uniformly dispersed GNPs through the matrix

$$g_{GNP}(z) = \mu_U W_{GNP}; \tag{15c}$$

μ_P, μ_L, and μ_U are the GNPs' gradient indices. The subscript P, L, and U are representatives of the words parabolic, linear, and uniform, respectively, where they are addressing different dispersion patterns of GNPs. For more information, it should be mentioned that the total GNPs content percentage plays a crucial role in GNPs dispersion pattern variations. For 0, 1/3, and 1 percentage of GNPs, the values of μ_P are 0, 1, and 3, respectively. The values of μ_L for 0, 1/3, and 1 percentage of GNPs are 0, 2/3, and 2, respectively. Also, for 0, 1/3, and 1 percentage of GNPs, the values of μ_U are 0, 1/3, and 1, respectively [68].

Moreover, other properties of the face sheets such as their Poisson's ratio, density, and hygrothermal expansion coefficients can be determined *via* the MR model as [69]:

$$\{\rho_f(z),\ \nu_f(z),\ \alpha_f(z),\ \beta_f(z)\} = \{\rho_{GNP},\ \nu_{GNP},\ \alpha_{GNP},\ \beta_{GNP}\}V_{GNP} + \{\rho_M,\ \nu_M,\ \alpha_M,\ \beta_M\}V_M \tag{16}$$

3 Motion equations

Hamilton's principle is used to extract the motion equations of the aforementioned sandwich shell [70]:

$$\delta \int_{t_1}^{t_2} (\Lambda - K - \Pi)\, \mathrm{d}t = 0 \tag{17}$$

in which Λ, K, and Π are whole strain energy, kinetic energy, and external work applied on the sandwich shell, respectively. Also, t is the time. Strain energy is due to the two face sheets and core and can be presented as:

$$\Lambda = \Lambda^{\mathrm{c}} + \Lambda^{\mathrm{f}} \tag{18}$$

The FG porous core strain energy is derived as:

$$\Lambda^{\mathrm{c}} = \frac{1}{2} \int_x \int_\theta \int_{-h_{\mathrm{c}}/2}^{+h_{\mathrm{c}}/2} [\sigma_{ij}^{\mathrm{c}} \varepsilon_{ij}]\, R\, \mathrm{d}z\, \mathrm{d}\theta\, \mathrm{d}x; \quad i, j = x, \theta, z \tag{19}$$

Furthermore, the strain energy of GNP-RC face sheets has the following form [71]:

$$\begin{aligned} \Lambda^{\mathrm{f}} = & \int_x \int_\theta \int_{(-h_{\mathrm{c}}/2)-(h_{\mathrm{b}})}^{-h_{\mathrm{c}}/2} 0.5\, [\sigma_{ij}^{\mathrm{f}} \varepsilon_{ij}]\, R \mathrm{d}z \mathrm{d}\theta \mathrm{d}x \\ & + \int_x \int_\theta \int_{+h_{\mathrm{c}}/2}^{(+h_{\mathrm{c}}/2)+(h_t)} 0.5\, [\sigma_{ij}^{\mathrm{f}} \varepsilon_{ij}]\, R \mathrm{d}z \mathrm{d}\theta \mathrm{d}x; \\ & i, j = x, \theta, z \end{aligned} \tag{20}$$

Therefore, the variations of the total strain energy can be presented as:

$$\begin{aligned} \delta\Lambda = & \int_x \int_\theta \left\{ \begin{array}{l} \left(-\frac{\partial}{\partial x} N_{xx} - \frac{1}{R} \frac{\partial}{\partial \theta} Q_{x\theta} \right) \delta u_0 + \left(-\frac{1}{R} \frac{\partial}{\partial \theta} N_{\theta\theta} - \frac{\partial}{\partial x} Q_{x\theta} \right) \delta v_0 \\ + \left(-\frac{\partial^2}{\partial x^2} G_{xx} - \frac{1}{R^2} \frac{\partial^2}{\partial \theta^2} G_{\theta\theta} + \frac{N_{\theta\theta}}{R} - \frac{1}{R} \frac{\partial}{\partial \theta} Q_{\theta z} + \frac{1}{R} \frac{\partial}{\partial \theta} G G_{\theta z} - \frac{\partial}{\partial x} Q_{xz} + \frac{\partial}{\partial x} G G_{xz} - \frac{2}{R} \frac{\partial^2}{\partial x \partial \theta} G_{x\theta} \right) \delta w_0 \\ + \left(-\frac{\partial}{\partial x} F_{xx} + F F_{xz} - \frac{1}{R} \frac{\partial}{\partial \theta} F_{x\theta} \right) \delta \lambda_x + \left(-\frac{1}{R} \frac{\partial}{\partial \theta} F_{\theta\theta} - \frac{\partial}{\partial x} F_{x\theta} + F F_{\theta z} \right) \delta \lambda_\theta \end{array} \right\} R \mathrm{d}\theta \mathrm{d}x \end{aligned} \tag{21}$$

where:

$$\left\{ \begin{array}{c} N_{\substack{xx \\ \theta\theta}} \\ F_{\substack{xx \\ \theta\theta}} \\ G_{\substack{xx \\ \theta\theta}} \end{array} \right\} = \left(Q_{\substack{11 \\ 12}} \begin{bmatrix} 1 & f & -g \\ f & f^2 & -fg \\ g & fg & -g^2 \end{bmatrix} + \frac{1}{R} Q_{\substack{12 \\ 22}} \begin{bmatrix} 1 & f & -g & 1 \\ f & f^2 & -fg & f \\ g & gf & -g^2 & g \end{bmatrix} \right) \left\{ \frac{\partial u_0}{\partial x} \quad \frac{\partial \lambda_x}{\partial x} \quad \frac{\partial^2 w_0}{\partial x^2} \quad \frac{\partial v_0}{\partial \theta} \quad \frac{\partial \lambda_\theta}{\partial \theta} \quad \frac{\partial^2 w_0}{\partial \theta^2} \quad w_0 \right\}^T, \tag{22a}$$

$$\left\{ \begin{array}{c} Q_{xz} \\ F F_{xz} \\ G G_{xz} \end{array} \right\} = Q_{55} \begin{bmatrix} 1 - g' & f' \\ f'(1 - g') & f'^2 \\ g'(1 - g') & g' f' \end{bmatrix} \left\{ \frac{\partial w_0}{\partial x} \quad \lambda_x \right\}^T, \tag{22b}$$

$$\left\{ \begin{array}{c} Q_{\theta z} \\ F_{\theta z} \\ G_{\theta z} \\ F F_{\theta z} \\ G G_{\theta z} \end{array} \right\} = Q_{44} \begin{bmatrix} f' - f & \frac{1}{R}\left(g + \frac{1}{R} g + 1 \right) & -\frac{1}{R} \\ f(f' - f) & \frac{f}{R}\left(g + \frac{1}{R} g + 1 \right) & -\frac{f}{R} \\ g(f' - f) & \frac{g}{R}\left(g + \frac{1}{R} g + 1 \right) & -\frac{g}{R} \\ f'(f' - f) & \frac{f'}{R}\left(g + \frac{1}{R} g + 1 \right) & -\frac{f'}{R} \\ g'(f' - f) & \frac{g'}{R}\left(g + \frac{1}{R} g + 1 \right) & -\frac{g'}{R} \end{bmatrix} \left\{ \lambda_\theta \quad \frac{\partial w_0}{\partial \theta} \quad v_0 \right\}^T, \tag{22c}$$

$$\begin{Bmatrix} Q_{x\theta} \\ F_{x\theta} \\ G_{x\theta} \end{Bmatrix} = Q_{66} \begin{bmatrix} 1 & f & -\frac{2}{R}g & \frac{1}{R} & \frac{1}{R}f \\ f & f^2 & -\frac{2}{R}fg & \frac{f}{R} & \frac{1}{R}f^2 \\ g & gf & -\frac{2}{R}g^2 & \frac{g}{R} & \frac{1}{R}fg \end{bmatrix} \begin{Bmatrix} \frac{\partial v_0}{\partial x} & \frac{\partial \lambda_\theta}{\partial x} & \frac{\partial^2 w_0}{\partial x \partial \theta} & \frac{\partial u_0}{\partial \theta} & \frac{\partial \lambda_x}{\partial \theta} \end{Bmatrix}^T \tag{22d}$$

Moreover, the definition of kinetic energy can be added as [35]:

$$K = \int_x \int_\theta \int_{-h/2}^{+h/2} 0.5\rho_{c,f}[(\partial u/\partial t)^2 + (\partial v/\partial t)^2 + (\partial w/\partial t)^2] R \mathrm{d}z \mathrm{d}\theta \mathrm{d}x \tag{23}$$

Using the variational approach, variations of the kinetic energy can be stated as:

$$\delta K = \int_x \int_\theta \begin{Bmatrix} \left(-I_0 \frac{\partial^2}{\partial t^2} u_0 - I_1 \frac{\partial^2}{\partial t^2} \lambda_x\right) \delta u_0 + \\ \left(-I_0 \frac{\partial^2}{\partial t^2} v_0 - I_1 \frac{\partial^2}{\partial t^2} \lambda_\theta + \frac{1}{R} I_1 \frac{\partial^3}{\partial \theta \partial t^2} w_0\right) \delta v_0 \\ + \begin{pmatrix} -I_2 \frac{\partial^3}{\partial x \partial t^2} u_0 - I_4 \frac{\partial^3}{\partial x \partial t^2} \lambda_x + I_5 \frac{\partial^4}{\partial x^2 \partial t^2} w_0 - \frac{1}{R} I_1 \frac{\partial^3}{\partial \theta \partial t^2} v_0 \\ -\frac{1}{R} I_3 \frac{\partial^3}{\partial \theta \partial t^2} \lambda_\theta + I_3 \frac{\partial^4}{\partial \theta^2 \partial t^2} w_0 - I_0 \frac{\partial^2}{\partial t^2} w_0 \end{pmatrix} \delta w_0 \\ + \left(-I_1 \frac{\partial^2}{\partial t^2} u_0 - I_3 \frac{\partial^2}{\partial t^2} \lambda_x + I_4 \frac{\partial^3}{\partial x \partial t^2} w_0\right) \delta \lambda_x \\ + \left(-I_1 \frac{\partial^2}{\partial t^2} v_0 - I_3 \frac{\partial^2}{\partial t^2} \lambda_\theta + \frac{I_3}{R} \frac{\partial^3}{\partial \theta \partial t^2} w_0\right) \delta \lambda_\theta \end{Bmatrix} R \mathrm{d}\theta \mathrm{d}x \tag{24}$$

in which:

$$I_0,\ I_1,\ I_2,\ I_3,\ I_4,\ I_5 = \int_{-\frac{h}{2}}^{\frac{h}{2}} \rho_{\mathrm{f},\ \mathrm{c}} (1,\ f,\ g,\ f^2,\ fg,\ g^2)\, \mathrm{d}z \tag{25}$$

Pasternak foundation is assumed for the sandwich shells. Therefore, external work due to the Pasternak foundation can be determined by ref. [72]:

$$\Pi_1 = \int_x \int_\theta 0.5 \left(-K_\mathrm{w} w_0^2 + K_\mathrm{g} w \{\partial^2 w_0/\partial x^2\} + \frac{1}{R^2} K_\mathrm{g} w \{\partial^2 w_0/\partial \theta^2\}\right) R \mathrm{d}\theta \mathrm{d}x \tag{26}$$

where K_w is the Winkler spring coefficient and K_g shows the shear layer coefficient.

The hygrothermal external work applied on the whole sandwich structure due to the hygrothermal load as a result of the temperature and moisture difference can be determined as follows [73,74]:

$$\Pi_2 = \int_x \int_\theta \left(0.5 \left\{ N_x^{HT} (\partial w_0/\partial x)^2 + \frac{1}{R^2} N_\theta^{HT} (\partial w_0/\partial \theta)^2 \right\}\right) R \mathrm{d}\theta \mathrm{d}x \tag{27}$$

where hygrothermal loads in x and θ directions are shown by N_x^{HT} and N_θ^{HT}, respectively, which can be presented as [10]:

$$\begin{aligned} N_x^{HT} &= \int_{-h/2}^{+h/2} (C_{11\ \mathrm{c,f}} + C_{12\ \mathrm{c,f}}) \alpha_{ij\ \mathrm{c,f}} \Delta T\ \mathrm{d}z \\ &\quad + \int_{-h/2}^{+h/2} (C_{11\ \mathrm{c,f}} + C_{12\ \mathrm{c,f}}) \beta_{ij\ \mathrm{c,f}} \Delta H\ \mathrm{d}z, \\ N_\theta^{HT} &= \int_{-h/2}^{+h/2} (C_{12\ \mathrm{c,f}} + C_{22\ \mathrm{c,f}}) \alpha_{ij\ \mathrm{c,f}} \Delta T\ \mathrm{d}z \\ &\quad + \int_{-h/2}^{+h/2} (C_{12\ \mathrm{c,f}} + C_{22\ \mathrm{c,f}}) \beta_{ij\ \mathrm{c,f}} \Delta H\ \mathrm{d}z \end{aligned} \tag{28}$$

Finally, whole external work's variations may be evaluated by summing the presented two works as:

$$\delta\Pi = \delta\Pi_1 + \delta\Pi_2 \tag{29}$$

So:

$$\delta\Pi = \int_x \int_\theta \left\{ \left(K_g \frac{\partial^2 w_0}{\partial x^2} + \frac{K_g}{R^2}\frac{\partial^2 w_0}{\partial \theta^2} - K_w w_0 + N_x^{HT}\frac{\partial^2 w_0}{\partial x^2} + \frac{N_\theta^{HT}}{R^2}\frac{\partial^2 w_0}{\partial \theta^2} \right) \delta w_0 \right\} R\,\mathrm{d}\theta\,\mathrm{d}x \tag{30}$$

By substituting equations (21), (24), and (30) into equation (17), the motion equations can be derived, setting the coefficients of δu_0, δv_0, δw_0, $\delta\lambda_x$, and $\delta\lambda_\theta$ to zero.

4 Analytical solution procedure

To solve the obtained differential equations, Navier's solution approach is applied. Based on this scheme, the geometrical boundary conditions for the simply supported type can be satisfied using the below functions for the displacement vectors [75]:

$$\begin{aligned}
u_0(x,\theta,t) &= \sum_{m=1}^{\infty}\sum_{n=1}^{\infty} U\cos(\alpha x)\sin(\beta\theta)\mathrm{e}^{\mathrm{i}\omega t},\\
v_0(x,\theta,t) &= \sum_{m=1}^{\infty}\sum_{n=1}^{\infty} V\sin(\alpha x)\cos(\beta\theta)\mathrm{e}^{\mathrm{i}\omega t},\\
w_0(x,\theta,t) &= \sum_{m=1}^{\infty}\sum_{n=1}^{\infty} W\sin(\alpha x)\sin(\beta\theta)\mathrm{e}^{\mathrm{i}\omega t},\\
\lambda_x(x,\theta,t) &= \sum_{m=1}^{\infty}\sum_{n=1}^{\infty} \Upsilon_x\cos(\alpha x)\sin(\beta\theta)\mathrm{e}^{\mathrm{i}\omega t},\\
\lambda_\theta(x,\theta,t) &= \sum_{m=1}^{\infty}\sum_{n=1}^{\infty} \Upsilon_\theta\sin(\alpha x)\cos(\beta\theta)\mathrm{e}^{\mathrm{i}\omega t}
\end{aligned} \tag{31}$$

where U, V, W, Y_x, and Y_θ denote the coefficients which are unknown. Also, $\alpha = n\pi/L$ and $\beta = m\pi/\varphi_r$ in which wavenumbers along x and θ directions are represented by n and m, respectively, which are integers. In the end, the motion equations can be obtained in a matrix form as:

$$([K]_{5\times5} - \omega^2[M]_{5\times5})\{UVW\Upsilon_x\Upsilon_\theta\}^T = 0 \tag{32}$$

The arrays of stiffness $[K]$ and mass $[M]$ matrices can be determined by substituting the functions of equation (31) into the governing motion equations which are obtained in the previous section. Solving equation (32) yields the natural frequencies of the studied structure.

5 Results and discussions

The current section is aimed to provide the results, in numerical and graphical form, to examine the vibrational behavior of the aforementioned sandwich shell under different conditions. The results will be reliable when the main code becomes validated with previous papers in this context. In this paper, the natural frequencies (in Hz) are listed for a single-layer orthotropic cylindrical shell with the following mechanical and geometrical specifications:

E_x = 120 GPa,	E_y = 10 GPa,	G_{xy} = 5.5 GPa,
ρ = 1,700 kg/m^3,	ν_x = 0.27,	ν_y = 0.0225,
R = 1 m,	h = 0.01 m,	L = 5 m

The cylindrical panel's different mode numbers' frequencies are obtained and compared with refs. [56,76] in Table 1. The results of reference papers are similar to the results acquired by the current code. Some partial errors may be in response to different displacement field utilizations, and also, different solution methods.

As another attempt to validate the results, the outcomes of this study are compared to those of Razavi *et al.* [27] and Ke *et al.* [26]. In these studies, the dimensionless natural frequency is achieved *via* $\omega R\sqrt{\rho(1-\nu^2)/E}$ in which $L/R = 20$, $h/R = 0.01$, and $\nu = 0.3$.

Therefore, the validity of the proposed method is confirmed. The vibrational behavior of the current sandwich cylindrical shell in response to different variable changes will be addressed in the following.

As previously mentioned, FG porous core is made of limestone, while the faces are fabricated from the GNP-reinforced epoxy. It is noted that for the limestone, E_0 = 25 GPa, ρ_0 = 2,700 kg/m^3, $\alpha_0 = 1.23\times10^{-5}$ 1/K, $\beta_0 = 2.43\times10^{-5}$ 1/K, and ν = 0.25 [77]. Furthermore, the properties of GNPs reinforcement and the epoxy matrix are listed below [67]:

E_{GNP} = 1.01 TPa,	ρ_{GNP} = 1062.5 kg/m^3,	ν_{GNP} = 0.186,
l_{GNP} = 2.5 μm,	w_{GNP} = 1.5 μm,	t_{GNP} = 1.5 nm,
$\alpha_{GNP} = 2.35\times10^{-5}$ 1/K,	$\beta_{GNP} = 4.35\times10^{-5}$ 1/K,	
E_M = 130 GPa,	ρ_M = 8, 960 kg/m^3,	ν_M = 0.34,
$\alpha_M = 60\times10^{-6}$ 1/K,	$\beta_M = 43\times10^{-6}$ 1/K	

Table 1: Comparing the results for a simpler state with those of previously published works (Hz)

Reference	(*m*,*n*)					
	(1,1)	(2,1)	(3,1)	(4,1)	(5,1)	(6,1)
Liu *et al.* (2012) (Exact)	741	416	258	198	209	266
Liu *et al.* (2012) (S-DQFME)	741	416	258	198	209	266
Mohammadimehr *et al.* (2019)	741.324	415.846	256.596	194.350	203.539	259.921
Current study	741.2861	415.1433	256.7928	194.456	203.468	260.157
Error (%)	0.0385	0.2063	0.4700	1.8214	2.6467	2.2455

Also, it must be noted that all the following results, except otherwise mentioned, are obtained with a porosity coefficient of 0.2 and for uniform GNPs dispersion and even pores distribution patterns (Table 2).

Figure 2 depicts natural frequency variations of the sandwich shell *versus* the porosity index. As it is evident, the higher porosity coefficients led to lower rigidity. As another expression and to provide a more physical point of view, it should be noted that higher values of porosity coefficients mean more holes and free spaces inside the core and cylindrical structures which is responsible for the lower stiffness and natural frequency, and higher flexibility. According to Figure 2, for the constant thickness of the sandwich cylindrical model, mid-radius enhancement decreased the natural frequency. Figure 3 illustrates the variation range of natural frequency *versus* length to thickness ratio (L/h) of the cylindrical sandwich shell. An increase in the mentioned ratio for constant total shell thickness implied an enhancement in the model length which can lead to the reduction of natural frequency and stiffness. Figure 3 also offers valuable information about the relationship of the porosity distribution patterns with the natural frequency of sandwich shell. It is clear that uniform and uneven distributions of porosity provide the lowest natural frequency and stiffness, respectively, due to pores' placement and its impact on the stiffness of the structure. The effects of W_{GNP} and h_c/h_f on natural frequency are displayed in Figure 4. At constant total thickness, an increase in the core thickness (i.e., a decline in the face sheets thickness) decremented the natural frequency and rigidity. Importantly, this reduction got steadier for higher values of porous core

Table 2: Comparing the dimensionless natural frequency for simply supported cylindrical shell with those of previously published works

Source	*m*			
	1	2	3	4
Razavi *et al.* (2017)	0.0161	0.0116	0.0248	0.0448
Ke *et al.* (2014)	0.0160	0.0093	0.0221	0.0420
Current study	0.0160	0.0104	0.0235	0.0435
Error (%)	0.625	9.057	5.531	2.987

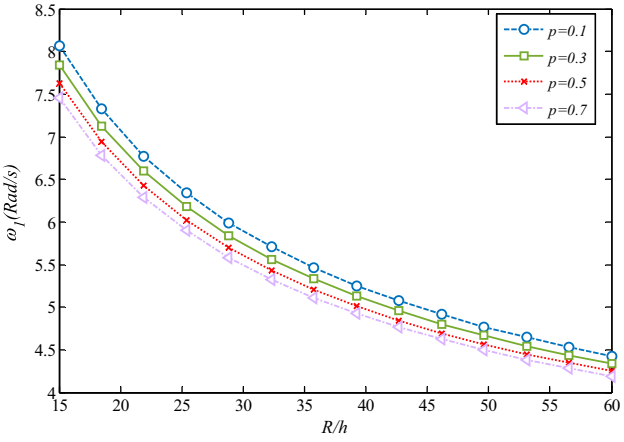

Figure 2: Effect of porosity coefficient and R/h ratio on the fundamental natural frequency ($h = 0.01m$, $h_c = 10h_f$, $L = 20h$, $\varphi_r = 2\pi$, $\mu_U = 1$).

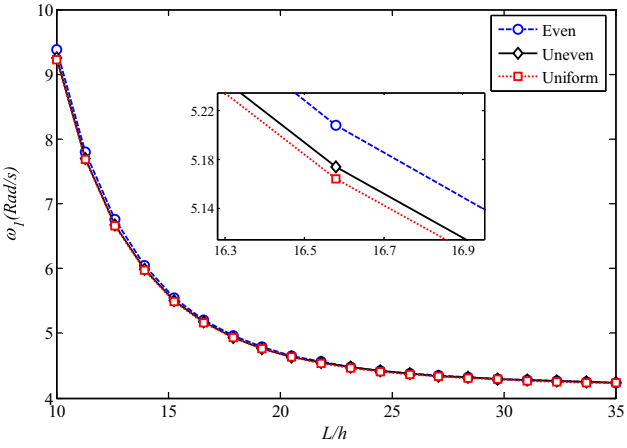

Figure 3: Porosity distribution pattern influence on the natural frequencies of the shell *versus* its aspect ratio ($h = 0.01m$, $h_c = 10h_f$, $L = 50h$, $\varphi_r = 2\pi$, $\mu_U = 1$).

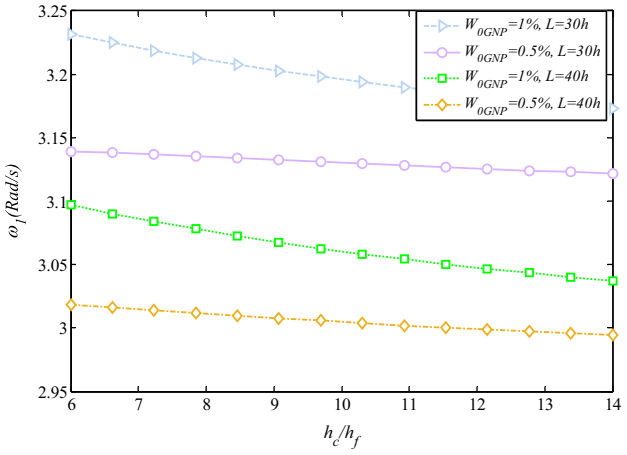

Figure 4: Thickness ratio and weight fraction of GNPs' effect on the results ($h = 0.01m$, $R = 100h$, $\varphi_r = 2\pi$, $\mu_P = 2$).

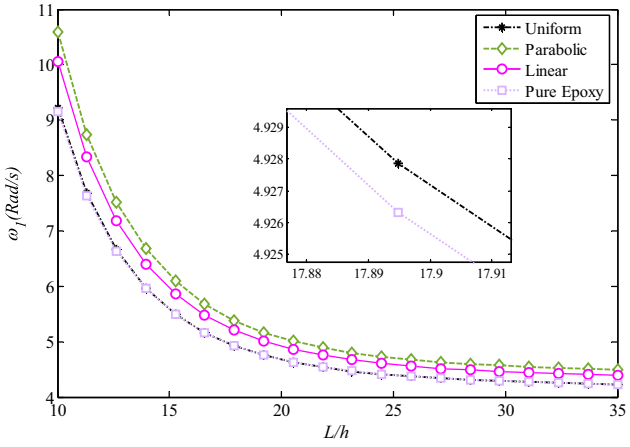

Figure 5: GNPs dispersion patterns' effect on the natural frequencies ($h = 0.01m$, $h_c = 10h_f$, $R = 100h$, $\varphi_r = 2\pi$).

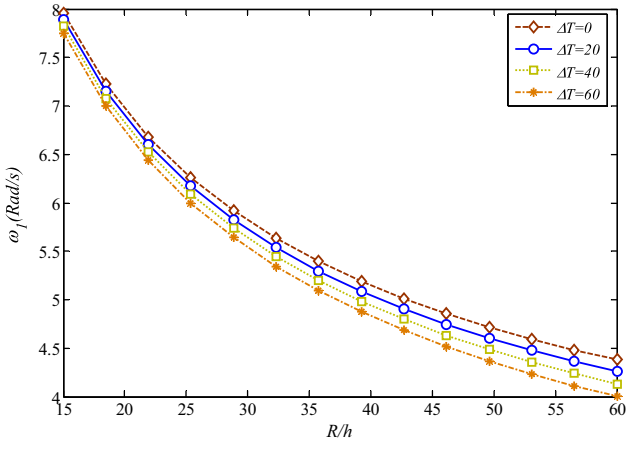

Figure 6: Temperature variations' effect on the vibration of the shell ($h = 0.01m$, $h_c = 10h_f$, $L = 20h$, $\varphi_r = 2\pi$, $\mu_U = 1$, $W_{GNP} = 0.01$).

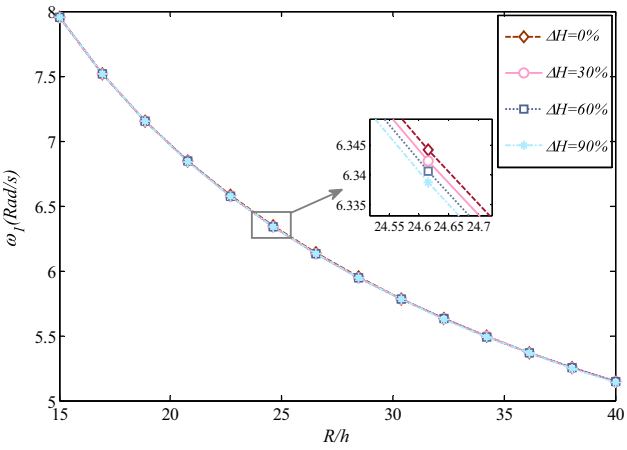

Figure 7: Moisture changes' influence on the structure's fundamental frequency ($h = 0.01m$, $h_c = 10h_f$, $L = 20h$, $\varphi_r = 2\pi$, $\mu_U = 1$).

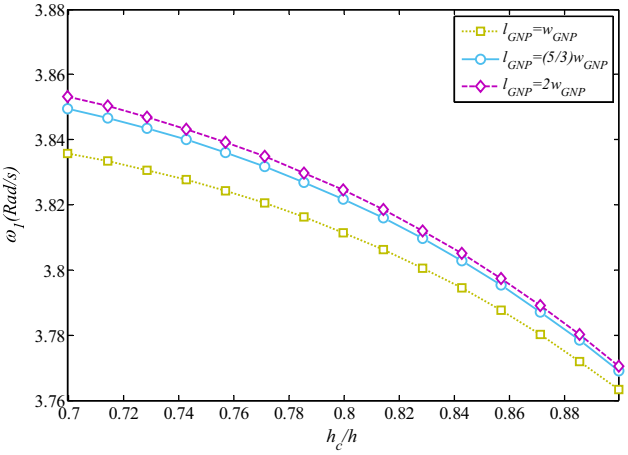

Figure 8: Effect of GNPs Geometrical parameters *versus* thicknesses of the layers ratio on the frequencies ($h = 0.01m$, $R = 100h$, $L = 20h$, $\varphi_r = 2\pi$, $\mu_P = 2$, $W_{GNP} = 1.5 \times 10^{-6}$).

thickness. In another conclusion, at constant GNPs length, higher values of W_{GNP} led to less rigid cylindrical sandwich shell structure. Moreover, Figure 5 presents the effect of different GNPs dispersion on natural frequency. Based on this figure, for similar GNPs dispersion coefficients, the parabolic dispersion of GNPs offered a stiffer structure. It means the highest natural frequency can be observed in the structures involving parabolic GNPs dispersion. Furthermore, comparing the epoxy curvature highlights the importance of GNPs presence as the reinforcing phase within the epoxy matrix. Figure 6 depicts natural frequency *versus* mid-radius to thickness ratio (R/h) of the shell for different temperature gradients. At the constant thickness of the sandwich cylindrical model, mid-radius enhancement decreased the natural

Table 3: Effect of pores' distribution pattern on the natural frequencies of the cylindrical shell for different wavenumbers

L/*h*	Porosity distribution pattern	(*m*,*n*)							
		(1,1)	(2,1)	(1,2)	(2,2)	(3,1)	(3,2)	(2,3)	(3,3)
10	Even	10.7268	10.9181	32.8658	33.1417	11.2085	33.5922	69.0011	69.4458
	Uneven	10.6144	10.7972	32.3807	32.6515	11.0746	33.0934	68.0454	68.4837
	Uniform	10.5919	10.7769	32.2801	32.5508	11.0576	32.9928	67.8365	68.2739
20	Even	6.9448	6.7601	10.7268	10.9181	6.3286	11.2085	19.9564	20.3801
	Uneven	6.9299	6.7376	10.6144	10.7972	6.2952	11.0746	19.6693	20.0826
	Uniform	6.9299	6.7353	10.5919	10.7769	6.2991	11.0576	19.6136	20.0281

Table 4: Effect of GNPs dispersion pattern on the frequencies of the cylindrical shell for various wavenumbers

L/*h*	GNPs dispersion pattern	(*m*,*n*)							
		(1,1)	(2,1)	(1,2)	(2,2)	(3,1)	(3,2)	(2,3)	(3,3)
10	Linear	11.5614	11.7791	35.9435	36.2448	12.1102	36.7365	75.2780	75.7588
	Parabolic	12.1246	12.3609	38.0393	38.3579	12.7207	38.8779	79.5004	80.0055
	Uniform	10.5919	10.7769	32.2801	32.5508	11.0576	32.9928	67.8365	68.2739
	Pure epoxy	9.3955	9.5379	27.5754	27.8062	9.7526	28.1831	58.1528	58.5329
20	Linear	7.2833	7.1048	11.5614	11.7791	6.6745	12.1102	21.7847	22.2513
	Parabolic	7.4928	7.3198	12.1246	12.3609	6.8929	12.7207	23.0332	23.5295
	Uniform	6.9230	6.7353	10.5919	10.7769	6.2991	11.0576	19.6136	20.0281
	Pure epoxy	6.4981	6.2979	9.3955	9.5379	6.0736	10.3616	18.1627	18.5484

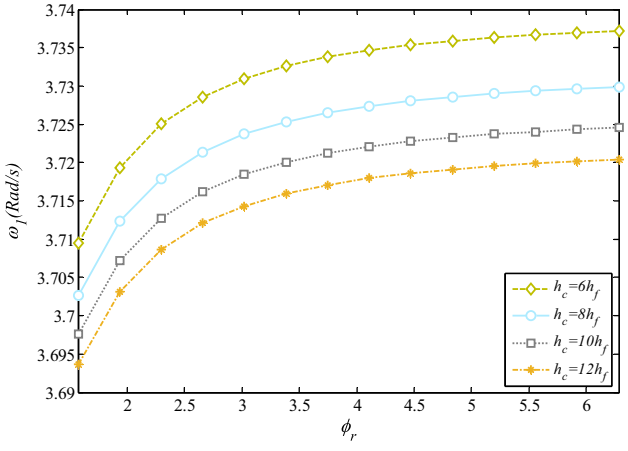

Figure 9: Rotation angle variations' effect on the fundamental natural frequency ($R = 100h$, $L = 20h$, $\varphi_r = 2\pi$, and $\mu_P = 2$).

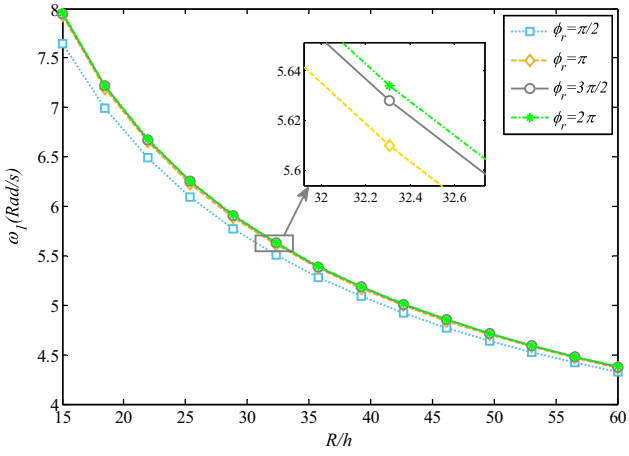

Figure 10: Influence of mid-radius to thickness and rotation angle on the shell's natural frequencies ($h = 0.01m$, $h_c = 10h_f$, $L = 20h$, and $\mu_U = 1$).

frequency. Such effect is visible for temperature difference enhancement and natural frequency, and consequently, stiffness reduction occurred due to the higher temperatures. The physical point of view is tangible when such structure initiates to melt due to the higher values of temperature differences. Natural frequency variation against humidity difference of surroundings is plotted in Figure 7 to illustrate the decline in the natural frequency, stiffness, and stability due to the humidity difference enhancement. The effect of different levels of moisture in the environment is negligible on the natural frequency of the whole cylindrical sandwich structure, but it can cause a crucial difference in the design of sensitive devices. Figure 8 presents the natural frequency *versus* GNPs geometrical dimensions. At constant GNPs

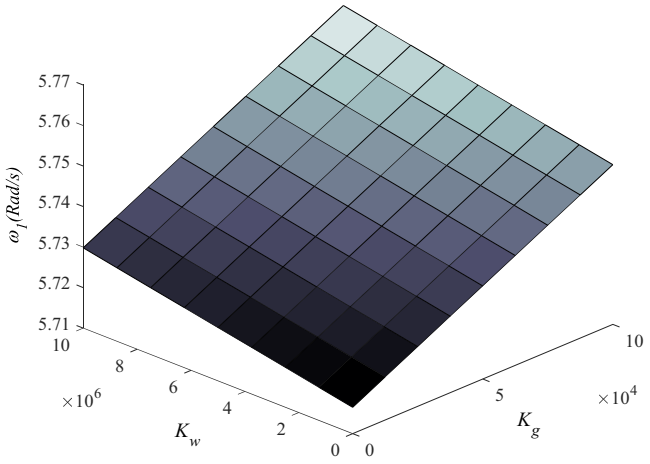

Figure 11: Pasternak foundation parameters' effect on the vibration of the cylindrical shell ($h = 0.01m$, $h_c = 10h$, $R = 100h$, $L = 20h$, $\varphi_r = 2\pi$, and $\mu_P = 2$).

width, natural frequency and stability increased by increasing the GNPs' length. Tables 3 and 4 are presented to provide a complete understanding of the effects of the mode number, pores dispersion, GNPs dispersion, and geometrical shape of the sandwich shell on natural frequency. For each condition, mode numbers of (2,2) and (1,1) led to the highest and lowest natural frequencies, respectively. Moreover, even dispersion of pores and parabolic dispersion of GNPs caused the highest magnitudes of natural frequency, stiffness, and stability for each mode. Table 3 is listed for $R = 20\ h$ and uniform GNPs dispersion pattern, while Table 4 is for uniform porosity distribution. Figure 9 investigates the influence of porous core thickness and rotation angle alternations on the cylindrical sandwich structure frequency. The whole structure thickness is kept constant and equal to 1 cm. Figure 10 shows the dependence of the natural frequency on the rotation angle of the cylindrical sandwich shell. As it is clear, the natural frequency and stability of the model deal with the rotation angle in the direct direction. As another expression, allocating lower values to the rotation angle led to lower natural frequency and instability for any radius to thickness ratio. By comparing Figures 9 and 10 what is novel in Figure 9 is the decline in the natural frequency due to the porous core thickness enhancement which resulted in stability reduction as well. Finally, in the last figure of this section, a 3-D figure is provided in Figure 11 to generate a comprehensive analysis of natural frequency variation *versus* foundation parameters. The stiffness and rigidity of the system decreased due to a reduction in the spring and shear layer constants.

6 Conclusion

SSDST, Navier's methods, and Hamilton's principle are used to derive and solve the governing equations of motion to assess the vibrational responses of a cylindrical sandwich shell including FG porous core and two FG-GNPRC face sheets. Different figures and tables are presented to address the physical properties such as stiffness, flexibility, and rigidity. It is observed that an enhancement in the GNPs' length and a decline in the porosity coefficient, humidity, and temperature differences can increment the natural frequency. The lowest natural frequency is observed in non-reinforced samples. At the constant shell thickness, lower natural frequencies, and consequently, stability are observed in higher shell radii. On the other hand, the rotation angle of the shell has a direct relationship with stiffness. These changes in the stiffness get intensified at the lower values of the shell radius and rotation angle of the shell. Based on these results, this paper tried to use the proposed cylindrical sandwich shell as a model for developing lighter and stiffer structures to use in the corresponding industries.

Funding information: This research is financially supported by the Ministry of Science and Technology of China (Grant No. 2019YFE0112400; 2018YFC1504303; 2017YFC0703603; 2017YFC1503103), National Science Foundation of China (Grant No. 52078310, 51878420), and the Key Research and Development Program of Liaoning Province (Grant No. 2017231010), the Taishan

Scholar Priority Discipline Talent Group program funded by the Shan Dong Province, and the first-class discipline project funded by the Education Department of Shandong Province.

Author contributions: All authors have accepted responsibility for the entire content of this manuscript and approved its submission.

Conflict of interest: The authors state no conflict of interest.

References

[1] Behdinan K, Moradi-Dastjerdi R, Safaei B, Qin Z, Chu F, Hui D. Graphene and CNT impact on heat transfer response of nanocomposite cylinders. Nanotechnol Rev. 2020;9:41–52. doi: 10.1515/ntrev-2020-0004.

[2] Huang Y, Zeng J. Recent development and applications of nanomaterials for cancer immunotherapy. Nanotechnol Rev. 2020;9:382–99. doi: 10.1515/ntrev-2020-0027.

[3] Wu Q, Miao WS, Zhang YD, Gao HJ, Hui D. Mechanical properties of nanomaterials: a review. Nanotechnol Rev. 2020;9:259–73. doi: 10.1515/ntrev-2020-0021.

[4] Yan Y, Nashath FZ, Chen S, Manickam S, Lim SS, Zhao H, et al. Synthesis of graphene: potential carbon precursors and approaches. Nanotechnol Rev. 2020;9:1284–314. doi: 10.1515/ntrev-2020-0100.

[5] Catania G, Strozzi M. Damping oriented design of thin-walled mechanical components by means of multi-layer coating technology. Coatings. 2018;8:73. doi: 10.3390/coatings8020073.

[6] Rongong JA, Goruppa AA, Buravalla VR, Tomlinson GR, Jones FR. Plasma deposition of constrained layer damping coatings. Proc Inst Mech Eng Part C J Mech Eng Sci. 2004;218:669–80. doi: 10.1243/0954406041319581.

[7] Yu L, Ma Y, Zhou C, Xu H. Damping efficiency of the coating structure. Int J Solids Struct. 2005;42:3045–58. doi: 10.1016/j.ijsolstr.2004.10.033.

[8] Amir S, Arshid E, Khoddami Maraghi Z, Loghman A, Ghorbanpour Arani A. Vibration analysis of magnetorheological fluid circular sandwich plates with magnetostrictive facesheets exposed to monotonic magnetic field located on visco-Pasternak substrate. J Vib Control. 2020;26:1523–37. doi: 10.1177/1077546319899203.

[9] Amir S, Arshid E, Khoddami Maraghi Z. Free vibration analysis of magneto-rheological smart annular three-layered plates subjected to magnetic field in viscoelastic medium. Smart Struct Syst. 2020;25:581–92. doi: 10.12989/sss.2020.25.5.581.

[10] Arshid E, Kiani A, Amir S. Magneto-electro-elastic vibration of moderately thick FG annular plates subjected to multi physical loads in thermal environment using GDQ method by considering neutral surface. Proc Inst Mech Eng Part L J Mater Des Appl. 2019;233:2140–59. doi: 10.1177/1464420719832626.

[11] Arshid E, Kiani A, Amir S, Zarghami Dehaghani M. Asymmetric free vibration analysis of first-order shear deformable functionally graded magneto-electro-thermo-elastic circular plates. Proc Inst Mech Eng Part C J Mech Eng Sci. 2019;233:5659–75. doi: 10.1177/0954406219850598.

[12] Koizumi M. FGM activities in Japan. Compos Part B Eng. 1997;28:1–4. doi: 10.1016/s1359-8368(96)00016-9.

[13] Liu GR, Han X, Lam KY. Integration technique for evaluating confluent hypergeometric functions and its application to functionally graded materials. Comput Struct. 2001;79:1039–47. doi: 10.1016/S0045-7949(00)00197-8.

[14] Han X, Liu GR, Lam KY. Transient waves in plates of functionally graded materials. Int J Numer Methods Eng. 2001;52:851–65. doi: 10.1002/nme.237.

[15] Najafizadeh MM, Eslami MR. Buckling analysis of circular plates of functionally graded materials under uniform radial compression. Int J Mech Sci. 2002;44:2479–93. doi: 10.1016/S0020-7403(02)00186-8.

[16] Arshid E, Khorshidvand AR. Free vibration analysis of saturated porous FG circular plates integrated with piezoelectric actuators *via* differential quadrature method. Thin-Walled Struct. 2018;125:220–33. doi: 10.1016/j.tws.2018.01.007.

[17] Huang KH, Dasgupta A. A layer-wise analysis for free vibration of thick composite cylindrical shells. J Sound Vib. 1995;186:207–22. doi: 10.1006/jsvi.1995.0444.

[18] Mahmoud Mousavi S, Aghdam MM. Static bending analysis of laminated cylindrical panels with various boundary conditions using the differential cubature method. J Mech Mater Struct. 2009;4:509–21. doi: 10.2140/jomms.2009.4.509.

[19] Pydah A, Batra RC. Analytical solution for cylindrical bending of two-layered corrugated and webcore sandwich panels. Thin-Walled Struct. 2018;123:509–19. doi: 10.1016/j.tws.2017.11.023.

[20] Sun G, Wang E, Zhang J, Li S, Zhang Y, Li Q. Experimental study on the dynamic responses of foam sandwich panels with different facesheets and core gradients subjected to blast impulse. Int J Impact Eng. 2020;135:103327. doi: 10.1016/j.ijimpeng.2019.103327.

[21] Arshid E, Arshid H, Amir S, Mousavi SB. Free vibration and buckling analyses of FG porous sandwich curved microbeams in thermal environment under magnetic field based on modified couple stress theory. Arch Civ Mech Eng. 2021;21:6. doi: 10.1007/s43452-020-00150-x.

[22] Barati MR, Sadr MH, Zenkour AM. Buckling analysis of higher order graded smart piezoelectric plates with porosities resting on elastic foundation. Int J Mech Sci. 2016;117:309–20. doi: 10.1016/j.ijmecsci.2016.09.012.

[23] Arshid E, Amir S, Loghman A. Thermal buckling analysis of FG graphene nanoplatelets reinforced porous nanocomposite MCST-based annular/circular microplates. Aerosp Sci Technol. 2021;106561. doi: 10.1016/j.ast.2021.106561.

[24] Salmani R, Gholami R, Ansari R, Fakhraie M. Analytical investigation on the nonlinear postbuckling of functionally graded porous cylindrical shells reinforced with graphene nanoplatelets. Eur Phys J Plus. 2021;136:1–19. doi: 10.1140/epjp/s13360-020-01009-z.

[25] Trabelsi S, Frikha A, Zghal S, Dammak F. A modified FSDT-based four nodes finite shell element for thermal buckling analysis of functionally graded plates and cylindrical shells.

Eng Struct. 2019;178:444–59. doi: 10.1016/j.engstruct.2018.10.047.
[26] Ke LL, Wang YS, Reddy JN. Thermo-electro-mechanical vibration of size-dependent piezoelectric cylindrical nanoshells under various boundary conditions. Compos Struct. 2014;116:626–36. doi: 10.1016/j.compstruct.2014.05.048.
[27] Razavi H, Babadi AF, Tadi Beni Y. Free vibration analysis of functionally graded piezoelectric cylindrical nanoshell based on consistent couple stress theory. Compos Struct. 2017;160:1299–309. doi: 10.1016/j.compstruct.2016.10.056.
[28] Khoa ND, Anh VM, Duc ND. Nonlinear dynamic response and vibration of functionally graded nanocomposite cylindrical panel reinforced by carbon nanotubes in thermal environment. J Sandw Struct Mater. 2019;1–32. doi: 10.1177/1099636219847191.
[29] Visconti P, Primiceri P, De Fazio R, Strafella L, Ficarella A, Carlucci AP. Light-Induced ignition of Carbon Nanotubes and energetic nano-materials: a review on methods and advanced technical solutions for nanoparticles-enriched fuels combustion. Rev Adv Mater Sci. 2020;59:26–46. doi: 10.1515/rams-2020-0010.
[30] Ahmad SI, Hamoudi H, Abdala A, Ghouri ZK, Youssef KM. Graphene-reinforced bulk metal matrix composites: synthesis, microstructure, and properties. Rev Adv Mater Sci. 2020;59:67–114. doi: 10.1515/rams-2020-0007.
[31] Sun Y, Sun Y, Peng Y, Zhou T, Liu H, Gao P. Study of the mechanical-electrical-magnetic properties and the microstructure of three-layered cement-based absorbing boards. Rev Adv Mater Sci. 2020;59:160–9. doi: 10.1515/rams-2020-0014.
[32] Hashim H, Salleh MS, Omar MZ. Homogenous dispersion and interfacial bonding of carbon nanotube reinforced with aluminum matrix composite: a review. Rev Adv Mater Sci. 2019;58:295–303. doi: 10.1515/rams-2019-0035.
[33] Arshid E, Khorasani M, Soleimani-Javid Z, Amir S, Tounsi A. Porosity-dependent vibration analysis of FG microplates embedded by polymeric nanocomposite patches considering hygrothermal effect *via* an innovative plate theory. Eng Comput. 2021;1–22. doi: 10.1007/s00366-021-01382-y.
[34] Fattahi AM, Safaei B, Ahmed NA. A comparison for the non-classical plate model based on axial buckling of single-layered graphene sheets. Eur Phys J Plus. 2019;134:1–13. doi: 10.1140/epjp/i2019-12912-7.
[35] Fattahi AM, Safaei B, Moaddab E. The application of nonlocal elasticity to determine vibrational behavior of FG nanoplates. Steel Compos Struct. 2019;32:281–92. doi: 10.12989/scs.2019.32.2.281.
[36] Mohseni A, Shakouri M. Natural frequency, damping and forced responses of sandwich plates with viscoelastic core and graphene nanoplatelets reinforced face sheets. Journal Vib Control. 2020;26:1165–77. doi: 10.1177/1077546319893453.
[37] Yaghoobi H, Taheri F. Analytical solution and statistical analysis of buckling capacity of sandwich plates with uniform and non-uniform porous core reinforced with graphene nanoplatelets. Compos Struct. 2020;252:112700. doi: 10.1016/j.compstruct.2020.112700.
[38] Kumar P, Srinivasa CV. On buckling and free vibration studies of sandwich plates and cylindrical shells: a review. J Thermoplast Compos Mater. 2020;33:673–724. doi: 10.1177/0892705718809810.
[39] Ibrahim HH, Tawfik M, Al-Ajmi M. Thermal buckling and nonlinear flutter behavior of functionally graded material panels. J Aircr. 2007;44:1610–8. doi: 10.2514/1.27866.
[40] Mehar K, Panda SK. Thermal free vibration behavior of FG-CNT reinforced sandwich curved panel using finite element method. Polym Compos. 2017. doi: 10.1002/pc.
[41] Karimiasl M, Ebrahimi F, Mahesh V. Nonlinear forced vibration of smart multiscale sandwich composite doubly curved porous shell. Thin-Walled Struct. 2019;143:106152. doi: 10.1016/j.tws.2019.04.044.
[42] Ramezani H, Mirzaei M. Transient elastodynamic behavior of cylindrical tubes under moving pressures and different boundary conditions. Appl Math Model. 2020;77:934–49. doi: 10.1016/j.apm.2019.08.011.
[43] Hebali H, Tounsi A, Houari MSA, Bessaim A, Bedia EAA. New Quasi-3D hyperbolic shear deformation theory for the static and free vibration analysis of functionally graded plates. J Eng Mech. 2014;140:374–83. doi: 10.1061/(ASCE)EM.1943-7889.0000665.
[44] Mirjavadi SS, Forsat M, Barati MR, Hamouda AMS. Investigating nonlinear forced vibration behavior of multi-phase nanocomposite annular sector plates using Jacobi elliptic functions. Steel Compos Struct. 2020;36:87–101. doi: 10.12989/scs.2020.36.1.087.
[45] Mirjavadi SS, Forsat M, Barati MR, Hamouda AMS. Nonlinear forced vibrations of multi-scale epoxy/CNT/fiberglass truncated conical shells and annular plates *via* 3D Mori-Tanaka scheme. Steel Compos Struct. 2020;35:765–77. doi: 10.12989/scs.2020.35.6.765.
[46] Safaei B. The effect of embedding a porous core on the free vibration behavior of laminated composite plates. Steel Compos Struct. 2020;35:659–70.
[47] Sahmani S, Fattahi AM, Ahmed NA. Analytical mathematical solution for vibrational response of postbuckled laminated FG-GPLRC nonlocal strain gradient micro-/nanobeams. Eng Comput. 2019;35:1173–89. doi: 10.1007/s00366-018-0657-8.
[48] Sahmani S, Aghdam MM. Axial postbuckling analysis of multilayer functionally graded composite nanoplates reinforced with GPLs based on nonlocal strain gradient theory. Eur Phys J Plus. 2017;132:1–17. doi: 10.1140/epjp/i2017-11773-4.
[49] Arshid E, Amir S. Size-dependent vibration analysis of fluid-infiltrated porous curved microbeams integrated with reinforced functionally graded graphene platelets face sheets considering thickness stretching effect. Proc Inst Mech Eng Part L J Mater Des Appl. 2021;235(5):146442072098555. doi: 10.1177/1464420720985556.
[50] Fan F, Xu Y, Sahmani S, Safaei B. Modified couple stress-based geometrically nonlinear oscillations of porous functionally graded microplates using NURBS-based isogeometric approach. Comput Methods Appl Mech Eng. 2020;372:113400. doi: 10.1016/j.cma.2020.113400.
[51] Wang YQ, Ye C, Zu JW. Nonlinear vibration of metal foam cylindrical shells reinforced with graphene platelets. Aerosp Sci Technol. 2019;85:359–70. doi: 10.1016/j.ast.2018.12.022.
[52] Qin Z, Pang X, Safaei B, Chu F. Free vibration analysis of rotating functionally graded CNT reinforced composite cylindrical shells with arbitrary boundary conditions. Compos Struct. 2019;220:847–60. doi: 10.1016/j.compstruct.2019.04.046.
[53] Qin Z, Chu F, Zu J. Free vibrations of cylindrical shells with arbitrary boundary conditions: a comparison study. Int J Mech Sci. 2017;133:91–9. doi: 10.1016/j.ijmecsci.2017.08.012.
[54] Shen HS, Xiang Y, Fan Y. Nonlinear vibration of functionally graded graphene-reinforced composite laminated cylindrical

shells in thermal environments. Compos Struct. 2017;182:447–56. doi: 10.1016/j.compstruct.2017.09.010.
[55] Amir S, Arshid E, Rasti-Alhosseini SMA, Loghman A. Quasi-3D tangential shear deformation theory for size-dependent free vibration analysis of three-layered FG porous micro rectangular plate integrated by nano-composite faces in hygro-thermal environment. J Therm Stress. 2020;43:133–56. doi: 10.1080/01495739.2019.1660601.
[56] Mohammadimehr M, Arshid E, Alhosseini SMAR, Amir S, Arani MRG. Free vibration analysis of thick cylindrical MEE composite shells reinforced CNTs with temperature-dependent properties resting on viscoelastic foundation. Struct Eng Mech. 2019;70:683–702. doi: 10.12989/sem.2019.70.6.683.
[57] Sahmani S, Aghdam MM, Bahrami M. Size-dependent axial buckling and postbuckling characteristics of cylindrical nanoshells in different temperatures. Int J Mech Sci. 2016;107:170–9. doi: 10.1016/j.ijmecsci.2016.01.014.
[58] Sahmani S, Safaei B. Large-amplitude oscillations of composite conical nanoshells with in-plane heterogeneity including surface stress effect. Appl Math Model. 2021;89:1792–813. doi: 10.1016/j.apm.2020.08.039.
[59] Khorasani M, Eyvazian A, Karbon M, Tounsi A, Lampani L, Sebaey TA. Magneto-electro-elastic vibration analysis of modified couple stress-based three-layered micro rectangular plates exposed to multi-physical fields considering the flexoelectricity effects. Smart Struct Syst. 2020;26:331–43. doi: 10.12989/sss.2020.26.3.331.
[60] Amir S, Arshid E, Ghorbanpour Arani MR. Size-dependent magneto-electro-elastic vibration analysis of FG saturated porous annular/circular micro sandwich plates embedded with nano-composite face sheets subjected to multi-physical pre loads. Smart Struct Syst. 2019;23:429–47. doi: 10.12989/sss.2019.23.5.429.
[61] Amir S, Soleimani-Javid Z, Arshid E. Size-dependent free vibration of sandwich micro beam with porous core subjected to thermal load based on SSDBT. Zeitschrift Fur Angew Math Und Mech. 2019;99:1–21. doi: 10.1002/zamm.201800334.
[62] Moradi-Dastjerdi R, Behdinan K, Safaei B, Qin Z. Buckling behavior of porous CNT-reinforced plates integrated between active piezoelectric layers. Eng Struct. 2020;222:222. doi: 10.1016/j.engstruct.2020.111141.
[63] Moradi-Dastjerdi R, Behdinan K, Safaei B, Qin Z. Static performance of agglomerated CNT-reinforced porous plates bonded with piezoceramic faces. Int J Mech Sci. 2020;188:105966. doi: 10.1016/j.ijmecsci.2020.105966.
[64] Arshid E, Amir S, Loghman A. Static and dynamic analyses of FG-GNPs reinforced porous nanocomposite annular microplates based on MSGT. Int J Mech Sci. 2020;180:105656. doi: 10.1016/j.ijmecsci.2020.105656.
[65] Safaei B, Khoda FH, Fattahi AM. Non-classical plate model for single-layered graphene sheet for axial buckling. Adv Nano Res. 2019;7:265–75. doi: 10.12989/anr.2019.7.4.265.
[66] Khorasani M, Soleimani-Javid Z, Arshid E, Lampani L, Civalek Ö. Thermo-elastic buckling of honeycomb micro plates integrated with FG-GNPs reinforced epoxy skins with stretching effect. Compos Struct. 2020;258:113430. doi: 10.1016/j.compstruct.2020.113430.
[67] Arefi M, Mohammad-Rezaei Bidgoli E, Rabczuk T. Thermo-mechanical buckling behavior of FG GNP reinforced micro plate based on MSGT. Thin-Walled Struct. 2019;142:444–59. doi: 10.1016/j.tws.2019.04.054.
[68] Arshid H, Khorasani M, Soleimani-Javid Z, Dimitri R, Tornabene F. Quasi-3D hyperbolic shear deformation theory for the free vibration study of honeycomb microplates with graphene nanoplatelets-reinforced epoxy skins. Molecules. 2020;25:5085. doi: 10.3390/molecules25215085.
[69] Thai CH, Ferreira AJM, Tran TD, Phung-Van P. A size-dependent quasi-3D isogeometric model for functionally graded graphene platelet-reinforced composite microplates based on the modified couple stress theory. Compos Struct. 2020;234:111695. doi: 10.1016/j.compstruct.2019.111695.
[70] Amir S, Khorasani M, BabaAkbar-Zarei H. Buckling analysis of nanocomposite sandwich plates with piezoelectric face sheets based on flexoelectricity and first-order shear deformation theory. J Sandw Struct Mater. 2018;22(7):109963621879538. doi: 10.1177/1099636218795385.
[71] Jouneghani FZ, Babamoradi H, Dimitri R, Tornabene F. A modified couple stress elasticity for non-uniform composite laminated beams based on the Ritz formulation. Molecules. 2020;25:1404. doi: 10.3390/molecules25061404.
[72] Kiani Y, Eslami MR. Thermal buckling and post-buckling response of imperfect temperature-dependent sandwich FGM plates resting on elastic foundation. Arch Appl Mech. 2012;82:891–905. doi: 10.1007/s00419-011-0599-8.
[73] Shen HS. Thermal buckling and postbuckling behavior of functionally graded carbon nanotube-reinforced composite cylindrical shells. Compos Part B Eng. 2012;43:1030–8. doi: 10.1016/j.compositesb.2011.10.004.
[74] Arshid E, Amir S, Loghman A. Bending and buckling behaviors of heterogeneous temperature-dependent micro annular/circular porous sandwich plates integrated by FGPEM nano-Composite layers. J Sandw Struct Mater. 2020;109963622095502. doi: 10.1177/1099636220955027.
[75] Amir S, BabaAkbar-Zarei H, Khorasani M. Flexoelectric vibration analysis of nanocomposite sandwich plates. Mech Based Des Struct Mach. 2020;48:146–63. doi: 10.1080/15397734.2019.1624175.
[76] Liu B, Xing YF, Qatu MS, Ferreira AJM. Exact characteristic equations for free vibrations of thin orthotropic circular cylindrical shells. Compos Struct. 2012;94:484–93.
[77] Detournay E, Cheng AH-D. Fundamentals of poroelasticity. Anal Des Methods. 1993;2:113–71. doi: 10.1016/B978-0-08-040615-2.50011-3.

Appendix

The arrays of stiffness and mass matrices in equation (32) are defined as:

$$K_{11} = Q_{110}\alpha^2 + \frac{Q_{660}\beta^2}{R^2},$$

$$K_{12} = \frac{1}{R}(Q_{120}\alpha\beta + Q_{660}\alpha\beta),$$

$$K_{13} = -Q_{112}\alpha^3 - \frac{Q_{122}\alpha\beta^2}{R^2} - \frac{Q_{120}\alpha}{R} - 2\frac{Q_{662}\alpha\beta^2}{R^2},$$

$$K_{14} = Q_{111}\alpha^2 + \frac{Q_{661}\beta^2}{R^2},$$

$$K_{15} = \frac{Q_{121}\alpha\beta}{R} + \frac{Q_{661}\alpha\beta}{R},$$

$$K_{21} = \frac{Q_{120}\alpha\beta}{R} + \frac{Q_{660}\alpha\beta}{R},$$

$$K_{22} = \frac{Q_{220}\beta^2}{R^2} + Q_{660}\alpha^2,$$

$$K_{23} = -\frac{Q_{122}\alpha^2\beta}{R} - \frac{Q_{222}\beta^3}{R^3} - \frac{Q_{220}\beta}{R^2} - 2\frac{Q_{662}\alpha^2\beta}{R},$$

$$K_{24} = \frac{Q_{121}\alpha\beta}{R} + \frac{Q_{661}\alpha\beta}{R},$$

$$K_{25} = \frac{Q_{221}\beta^2}{R^2} + Q_{661}\alpha^2,$$

$$K_{31} = -Q_{112}\alpha^3 - \frac{Q_{122}\alpha\beta^2}{R^2} - \frac{Q_{120}\alpha}{R} - 2\frac{Q_{662}\alpha\beta^2}{R^2},$$

$$K_{32} = -\frac{Q_{122}\alpha^2\beta}{R} - \frac{Q_{222}\beta^3}{R^3} - \frac{Q_{220}\beta}{R^2} - 2\frac{Q_{662}\alpha^2\beta}{R},$$

$$K_{33} = 2\frac{Q_{122}\alpha^2}{R} + 4\frac{Q_{665}\alpha^2\beta^2}{R^2} + 2\frac{Q_{125}\alpha^2\beta^2}{R^2} + \frac{Q_{220}}{R^2} + Q_{115}\alpha^4 + Q_{550}\alpha^2 - 2Q_{559}\alpha^2 + Q_{5511}\alpha^2 + \frac{Q_{225}\beta^4}{R^4} + 2\frac{Q_{222}\beta^2}{R^3} + \frac{Q_{440}\beta^2}{R^2} - 2\frac{Q_{449}\beta^2}{R^2} + \frac{Q_{4411}\beta^2}{R^2} + K_g\alpha^2 + \frac{1}{R^2}K_g\beta^2 + K_w + \frac{1}{R^2}N_\theta^{HT}\beta^2 + N_x^{HT}\alpha^2,$$

$$K_{34} = -2\frac{Q_{664}\alpha\beta^2}{R^2} - \frac{Q_{124}\alpha\beta^2}{R^2} - Q_{114}\alpha^3 + Q_{556}\alpha - Q_{5510}\alpha - \frac{Q_{121}\alpha}{R},$$

$$K_{35} = -\frac{Q_{124}\alpha^2\beta}{R} - 2\frac{Q_{664}\alpha^2\beta}{R} - \frac{Q_{224}\beta^3}{R^3} - \frac{Q_{221}\beta}{R^2} + \frac{Q_{446}\beta}{R} - \frac{Q_{4410}\beta}{R},$$

$$K_{41} = Q_{111}\alpha^2 + \frac{Q_{661}\beta^2}{R^2},$$

$$K_{42} = \frac{Q_{121}\alpha\beta}{R} + \frac{Q_{661}\alpha\beta}{R},$$

$$K_{43} = -2\frac{Q_{664}\alpha\beta^2}{R^2} - \frac{Q_{124}\alpha\beta^2}{R^2} - Q_{114}\alpha^3 + Q_{556}\alpha - Q_{5510}\alpha - \frac{Q_{121}\alpha}{R},$$

$$K_{44} = -2\frac{Q_{664}\alpha\beta^2}{R^2} - \frac{Q_{124}\alpha\beta^2}{R^2} - Q_{114}\alpha^3 + Q_{556}\alpha - Q_{5510}\alpha - \frac{Q_{121}\alpha}{R},$$

$$K_{45} = \frac{Q_{123}\alpha\beta}{R} + \frac{Q_{663}\alpha\beta}{R},$$

$$K_{51} = \frac{Q_{121}\alpha\beta}{R} + \frac{Q_{661}\alpha\beta}{R},$$

$$K_{52} = \frac{Q_{221}\beta^2}{R^2} + Q_{661}\alpha^2,$$

$$K_{53} = \frac{1}{R}\left(-Q_{124}\alpha^2\beta - 2Q_{664}\alpha^2\beta - \frac{Q_{224}\beta^3}{R^2} - \frac{Q_{221}\beta}{R} + Q_{446}\beta - Q_{4410}\beta\right),$$

$$K_{54} = \frac{Q_{123}\alpha\beta}{R} + \frac{Q_{663}\alpha\beta}{R},$$

$$K_{55} = \frac{Q_{223}\beta^2}{R^2} + Q_{663}\alpha^2 + Q_{448},$$

$$\begin{aligned}
&M_{11} = I_0, \quad M_{21} = 0, \quad M_{31} = -I_2\alpha,\\
&M_{12} = 0, \quad M_{22} = I_0, \quad M_{32} = -I_1\beta/R,\\
&M_{13} = 0, \quad M_{23} = -I_1\beta/R, \quad M_{33} = I_5\alpha^2 + I_3\beta^2 + I_0,\\
&M_{14} = I_1, \quad M_{24} = I_1, \quad M_{34} = -I_4\alpha,\\
&M_{15} = 0, \quad M_{25} = 0, \quad M_{35} = -I_3\beta/R,
\end{aligned}$$

$$\begin{aligned}
&M_{41} = I_1, \quad M_{51} = 0,\\
&M_{42} = 0, \quad M_{52} = I_1,\\
&M_{43} = -I_4\alpha, \quad M_{53} = -I_3\beta/R,\\
&M_{44} = I_3, \quad M_{54} = 0,\\
&M_{45} = 0, \quad M_{55} = I_3
\end{aligned}$$

in which:

$$Q_{110}, Q_{111}, Q_{112}, Q_{113}, Q_{114}, Q_{115} = \int_{-\frac{h}{2}}^{\frac{h}{2}} C_{11}(z)(1, f(z), g(z), f(z)^2, f(z)g(z), g(z)^2)\,\mathrm{d}z$$

$$Q_{120}, Q_{121}, Q_{122}, Q_{123}, Q_{124} = \int_{-\frac{h}{2}}^{\frac{h}{2}} C_{12}(z)(1, f(z), g(z), f(z)^2, f(z)g(z))\mathrm{d}z$$

$$Q_{220}, Q_{221}, Q_{223} = \int_{-\frac{h}{2}}^{\frac{h}{2}} C_{22}(z)(1, f(z), f(z)^2)\mathrm{d}z$$

$$Q_{440}, Q_{441}, Q_{443}, Q_{446}, Q_{447}, Q_{448} = \int_{-\frac{h}{2}}^{\frac{h}{2}} C_{44}(z)(1, f(z), f(z)^2, f(z)', f(z)'f(z), f(z)'^2)\mathrm{d}z$$

$$Q_{550}, Q_{556}, Q_{558}, Q_{559}, Q_{5510}, Q_{5511} = \int_{-\frac{h}{2}}^{\frac{h}{2}} C_{55}(z)(1, f(z)', f(z)'^2, g(z)', f(z)'g(z)', g(z)'^2)\mathrm{d}z$$

$$Q_{660}, Q_{661}, Q_{662}, Q_{663}, Q_{664}, Q_{665} = \int_{-\frac{h}{2}}^{\frac{h}{2}} C_{66}(z)(1, f(z), g(z), f(z)^2, f(z)g(z), g(z)^2)\mathrm{d}z$$